Supporting Information

Enhanced Ion Conductivity of "Water-in-Salt" Electrolytes by Nanochannel Membranes

Yuqi Wang, ‡[ab] Xishun Hao, ‡[c] Yuan Kang,[d] Mengyang Dong,[a] Zhou Fang,[ab] Yue Hu,[ab] Huanting Wang,[d] Xiulin Fan,*[a] Youguo Yan,*[c] Zhizhen Ye,[ab] Xinsheng Peng*[ab]

[a.] State Key Laboratory of Silicon Materials, School of Materials Science and Engineering, Zhejiang University, Hangzhou, 310027, Chin. E-mail: pengxinsheng@zju.edu.cn; xlfan@zju.edu.cn

[b.] Wenzhou Key Laboratory of Novel Optoelectronic and Nanomaterials, Institute of Wenzhou, Zhejiang University, Wenzhou 325006, China.

[c.] *School of Materials Science and Engineering, China University of Petroleum, Qingdao, 266580, China*. E-mail: yyg@upc.edu.cn

[d.] Department of Chemical Engineering, Monash University, Clayton, Victoria 3800, Australia

‡ These authors contributed equally to this work.

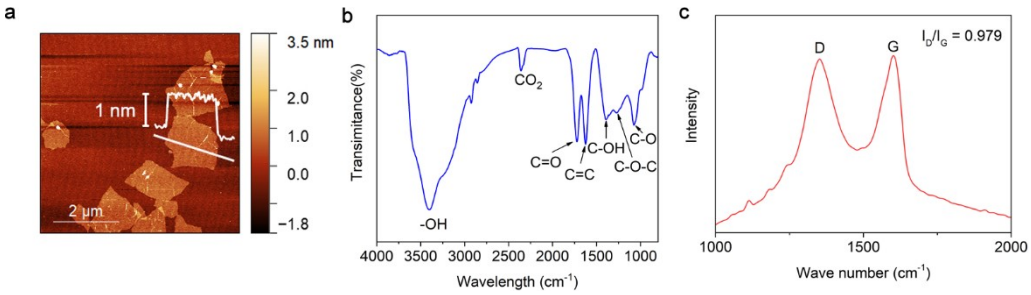

Fig. S1 Characterization of GO nanosheets and membrane. (a) Atomic force microscope (AFM) image of exfoliated GO. (b) FTIR spectrum of GO membrane. (c) Raman spectrum of GO membrane.

The as-prepared GO nanosheets show a single-layer thickness of 1 nm and lateral sizes ranging from hundreds of nanometers to a few microns under atomic force microscopy, which is a typical single-layer GO. Typical oxygen functional groups on GO nanosheets were identified by Fourier transform infrared (FTIR) spectroscopy, which suggested the presence of hydroxyl groups (–OH stretching at 3400 cm^{-1}), carboxyl groups (C=O stretching at 1720 cm^{-1} and C–OH stretching at 1390 cm^{-1}), unoxidized C=C bonds (stretching at 1622 cm^{-1}), epoxy groups (C–O–C stretching at 1260 cm^{-1}), alkoxy groups (C–O stretching at 1070 cm^{-1}), and absorbs CO_2 at 2360 cm^{-1}. These results corresponded with the findings of previous studies and enable the nanosheets to be well-dispersed in colloids for further processing.[1,2] Based on the Raman analysis, the main characteristic D and G bands of GO can be seen clearly at 1350 and 1600 cm^{-1}, respectively.

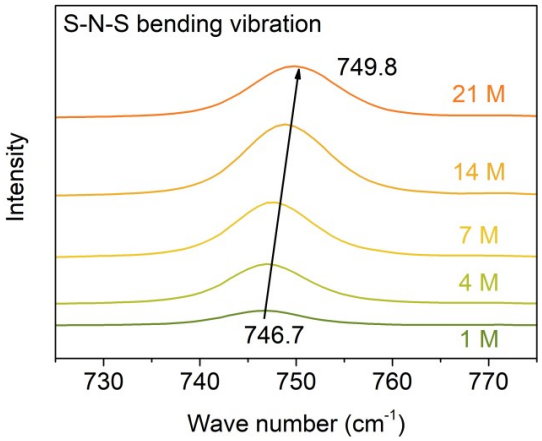

Fig. S2 Progression of Raman vibration at ~744 cm^{-1} of S-N-S bending vibration with LiTFSI concentration.

Various concentration of LiTFSI aqueous electrolytes has been prepared and their saturated concentration is 21 M at room temperature. The S−N−S bond of LiTFSI Raman shifts means the formation of a percolated $TFSI^-$ anionic network in the highly concentrated electrolytes.[3]

Table S1. X-ray photoelectron spectra (XPS) Contents of C1s, F1s, N1s, O1s, and S2p of GO membrane embedded with various concentrations of LiTFSI electrolytes.

	Mol/kg	***0***	***1***	***4***	***7***	***14***	***21***
	BE (eV)	Atomic%					
C1s	285.72	73.82	33.14	31.49	27.7	18.19	5.36
F1s	687.84	N/A	23	30.11	28.86	34.3	45.09
N1s	398.83	N/A	4.14	4.85	5	6.11	6.69
O1s	532.04	26.18	32.48	30.66	30.12	30.58	29.27
S2p	168.77	N/A	7.25	7.52	8.32	10.83	13.50

The contents of C1s and O1s are decreased while the F1s N1s O 1s and S2p are increased with the concentration increasing.

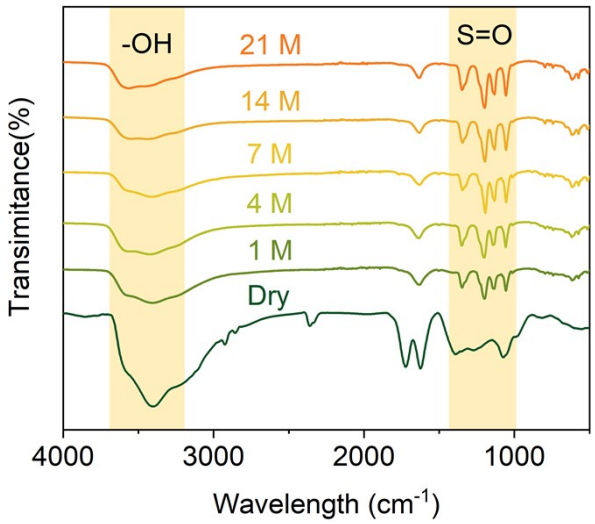

Fig. S3 FTIR spectra of GO membrane embedded with different concentrations of LiTFSI electrolytes.

The yellow background track stretching vibration changes in the S=O vibrations (~1120 cm^{-1}) of $TFSI^-$ and -OH vibrations (~3350 cm^{-1}) of water molecules. The intensity of these -OH peaks decreases while S=O peaks increase with the ascending of salt concentration.

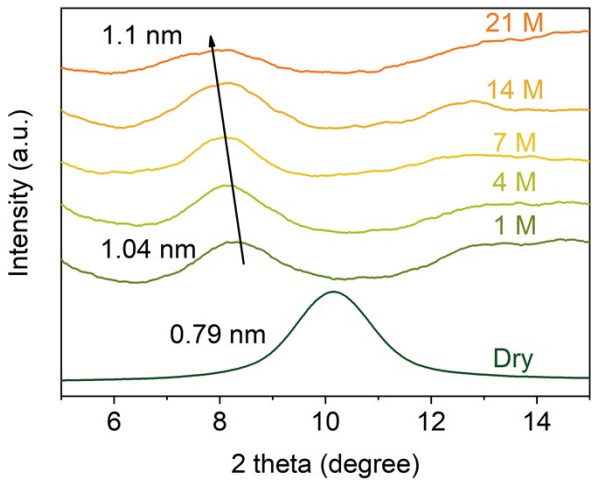

Fig. S4 X-ray diffraction (XRD) patterns of GO membranes infiltered with different concentrations of LiTFSI electrolytes after two weeks.

After two weeks, the interlayer spacing of GO membranes containing LiTFSI exhibited little difference compared with the fresh membranes. This good stability indicates the concentrated electrolytes are able to help GO membrane anti-swell.

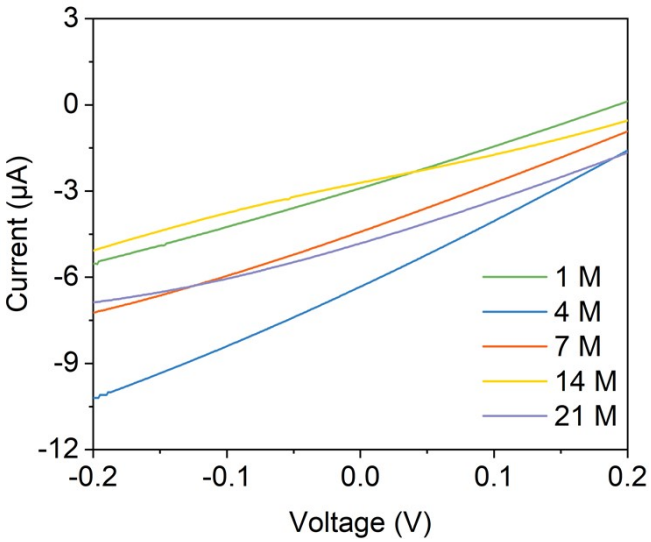

Fig. S5 Current-voltage (I−V) curves were recorded at different LiTFSI concentrations (1 M, 4 M, 7 M, 14 M, 21 M).

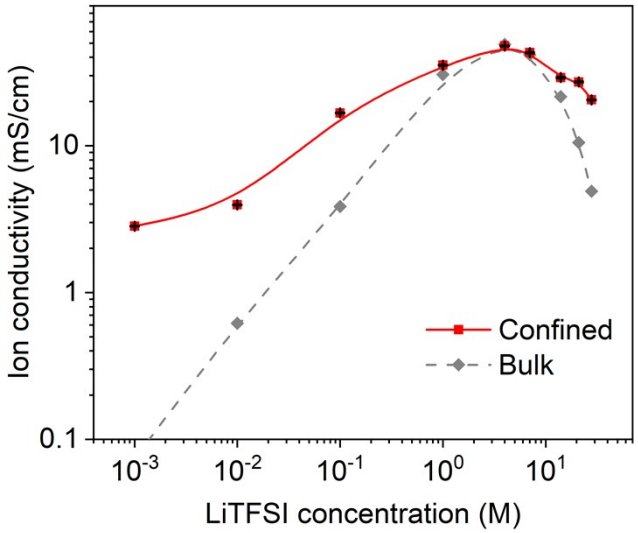

Fig. S6 Ionic conductivity measurements with varying LiTFSI concentrations of bulk and two GO membrane-based devices. The curves are guides for the eye.

At low concentrations, the GO conduits show a greatly enhanced ionic conductivity than the bulk system. This represents a typical surface-charge governed ionic conductivity caused by strong Debye overlap. For monovalent electrolytes, the equation of Debye length λ_D is shown below:[4,5]

$$\lambda_D = \left(\frac{\varepsilon_r \varepsilon_0 kT}{2e^2 N_a C}\right)^{\frac{1}{2}} \quad (1)$$

where ε_r is the dielectric constant of the solvent, ε_0 is vacuum permittivity, k is the Boltzman constant, T is absolute temperature, e is the charge of an electron, N_a is the Avogadro number, and C is the concentration in moles per m^3. For 0.1 M LiTFSI electrolyte, the Debye screening length is about 1 nm which is comparable to the nanochannel size.[6,7] Therefore, it begins to deviate from bulk behavior and gradually plateaus at lower concentrations, showing the characteristic surface-charge-governed ionic transport.[8,9]

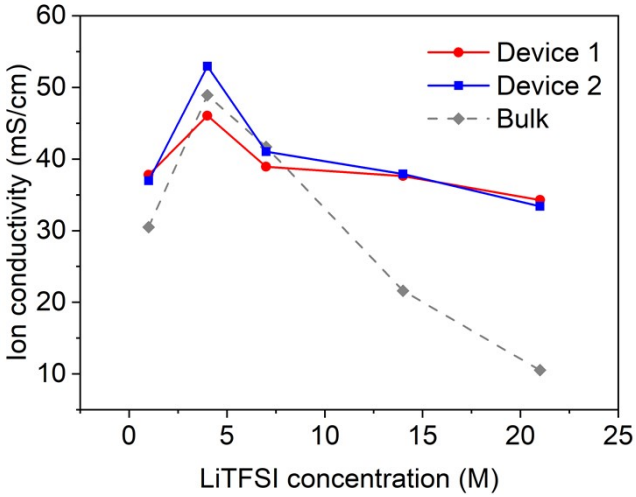

Fig. S7 Ionic conductivity measurements with varying concentrations of bulk and two GO membrane-based devices.

These two devices have a similar area of ~ 11 mm × 7 mm (length × width) with different thicknesses (2 μm and 6 μm) showing consistent and reproducible behavior in LiTFSI.

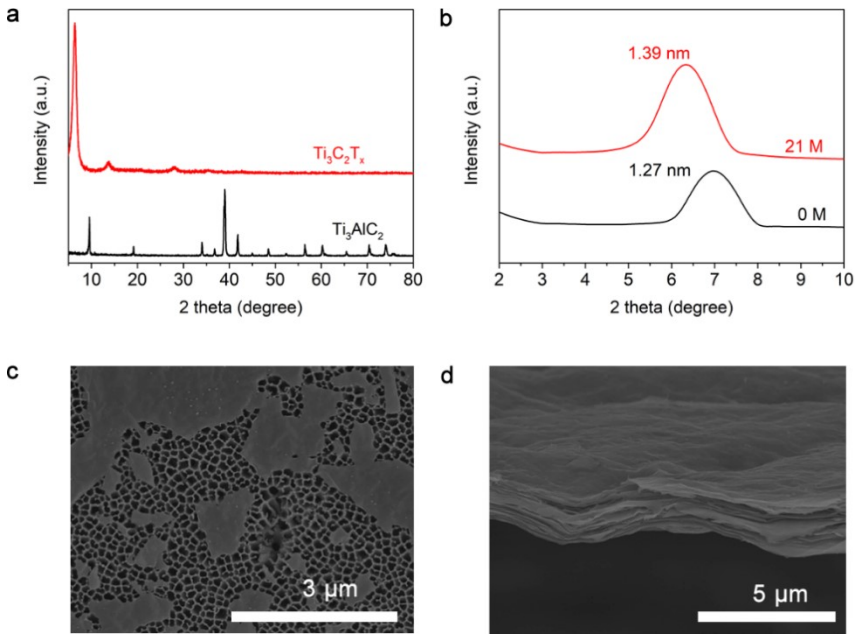

Fig. S8 Characterization of $Ti_3C_2T_x$ nanosheets and membrane. (a) XRD pattern of $Ti_3C_2T_x$ (MXene) and Ti_3AlC_2 (MAX) powder. (b) XRD patterns of dry MXene membrane and MXene membrane immersed in 21 M LiTFSI electrolyte. Scanning electron microscopy (SEM) characterization of the MXene nanosheets (c) on anodic aluminum oxide (AAO) substrate and (d) cross-section of layered MXene membrane.

After the exfoliation process, the diffraction peak of the (104) planes of Ti_3AlC_2 (MAX) located at 39° was absent in the pattern of $Ti_3C_2T_x$ (MXene), demonstrating the successful removal of the Al layers by etching. The XRD peak shifting after being immersed in the electrolyte indicates that the interlayer spacing of the MXene membrane swells from 1.27 to 1.39 nm.

SEM images showed the as-prepared nanosheets have lateral sizes ranging from hundreds of nanometers to a few microns and the cross-section confirms the formation of well-stacked MXene layers. A porous network consisting of interconnected nanochannels was thus formed and was able to sustain the transport of water and ions.

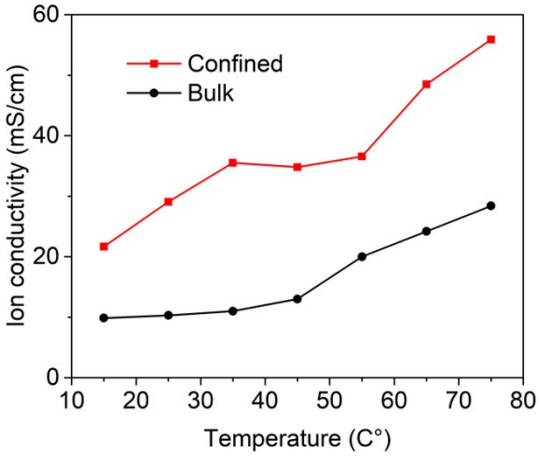

Fig. S9. Ionic conductivity as a function of temperature in bulk and GO membrane in 21 M LiTFSI electrolyte. The test is conducted on a hot plate with a thermometer inserted into the electrolyte from 15°C (crystal state) to 75°C, showing an increasing trend.

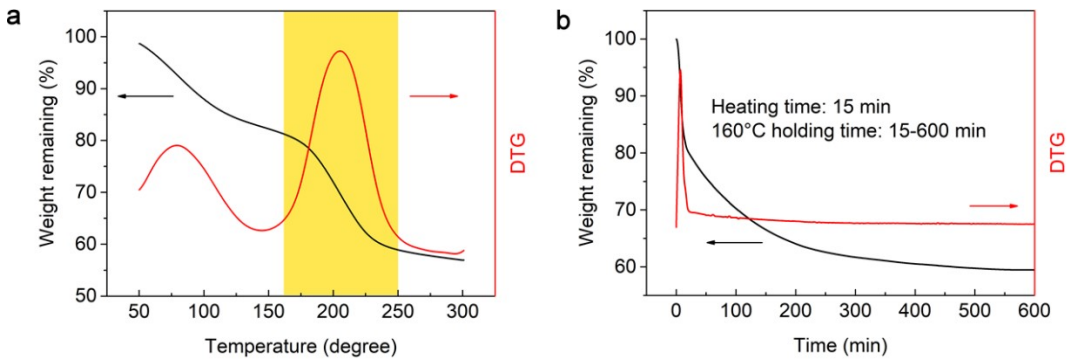

Fig. S10 Thermal behavior of GO membranes. (a) TGA of GO membranes while changing the temperature from 30 to 300 °C. (b) TGA of GO membranes undergoing heat treatment at 160 °C.

Thermogravimetric analyzer (TGA) results display GO membrane weight loss heating from 30 to 300°C. The losing weight under 100 °C is mainly because of the evaporating of the absorbed water inside GO. The removal of oxygen-containing functional groups accelerates after 100 °C, especially between 150~250 °C, which is the same as reported.[10] In this work, to avoid the huge changing in nanosheet structure and interlayer spacing, 160 °C was chosen as the heat-treatment temperature for generating prGO membranes. A very slow rate of removal of oxygen-containing functional groups was observed while holding the reaction at 160 °C for 10 h, indicating that the degree of reduction of GO can be adjusted by heat treatment at different holding times.

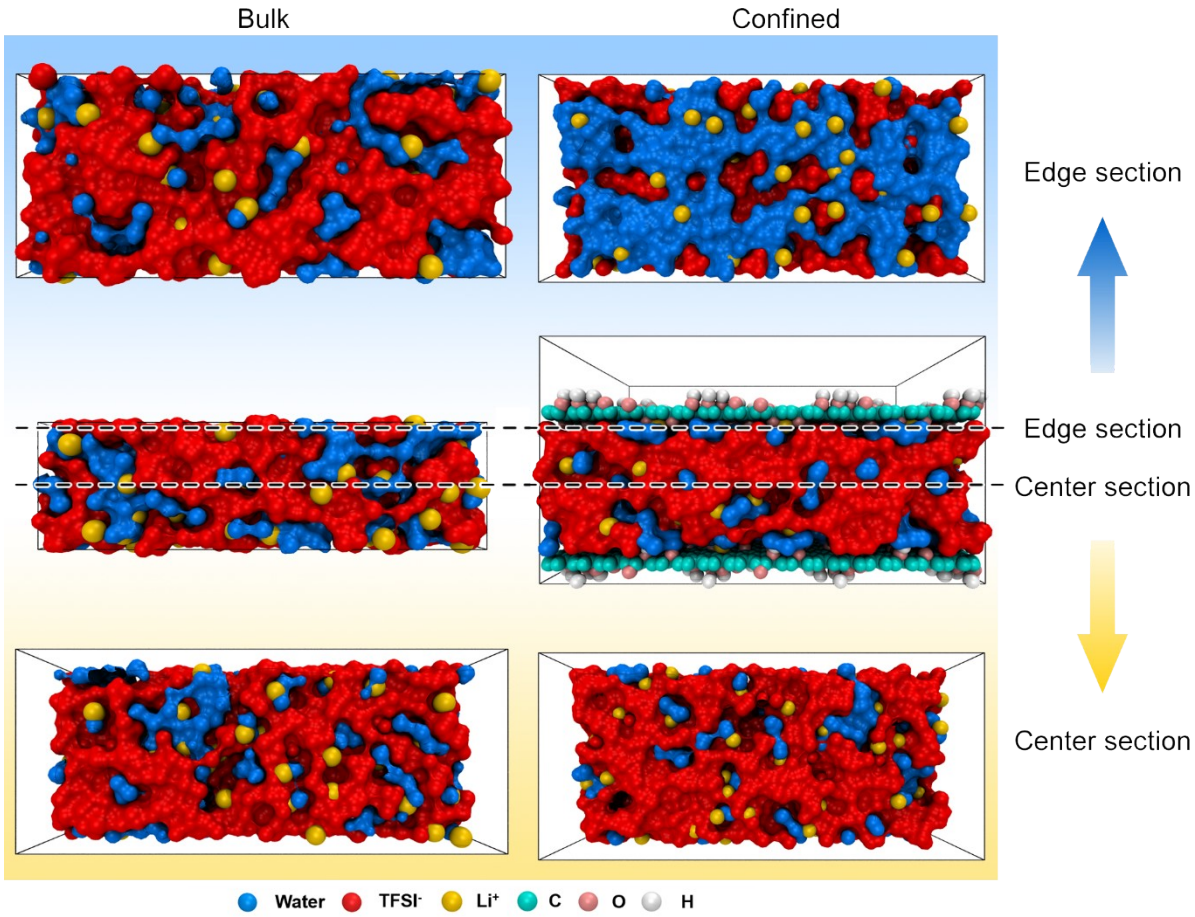

Fig. S11 Molecular dynamic simulation models for bulk (left) and confined (right) 21 M LiTFSI electrolyte systems; Top view of edge section (near channel walls) in bulk and confined; Top view of the center section (away channel walls) in bulk and confined.

The top view of the edge section and center section for both bulk and confined model has been displayed. A more continuous water/anion channel was observed in the confined model on the edge/center section respectively.

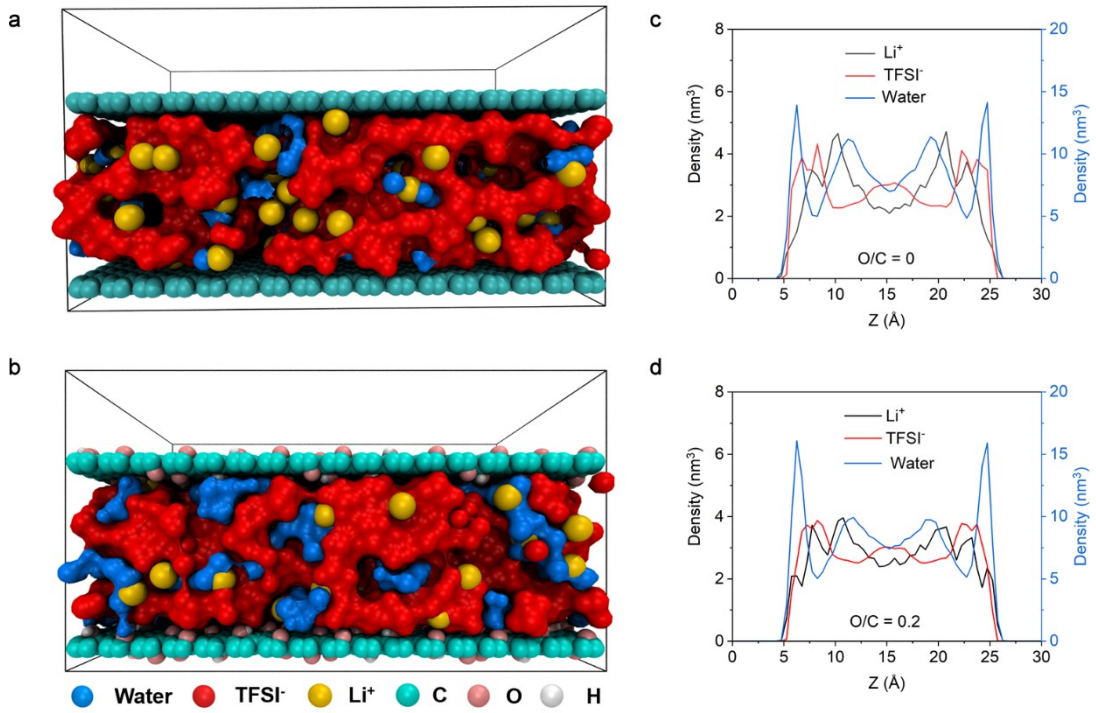

Fig. S12 (a-b) Molecular dynamic simulation models and (c-d) distribution characteristics and of cation, anion and water in nanoconfined 21 M LiTFSI electrolyte along the direction perpendicular to the prGO nanosheet with the number of (a, c) O/C = 0 and (b, d) O/C = 0.2.

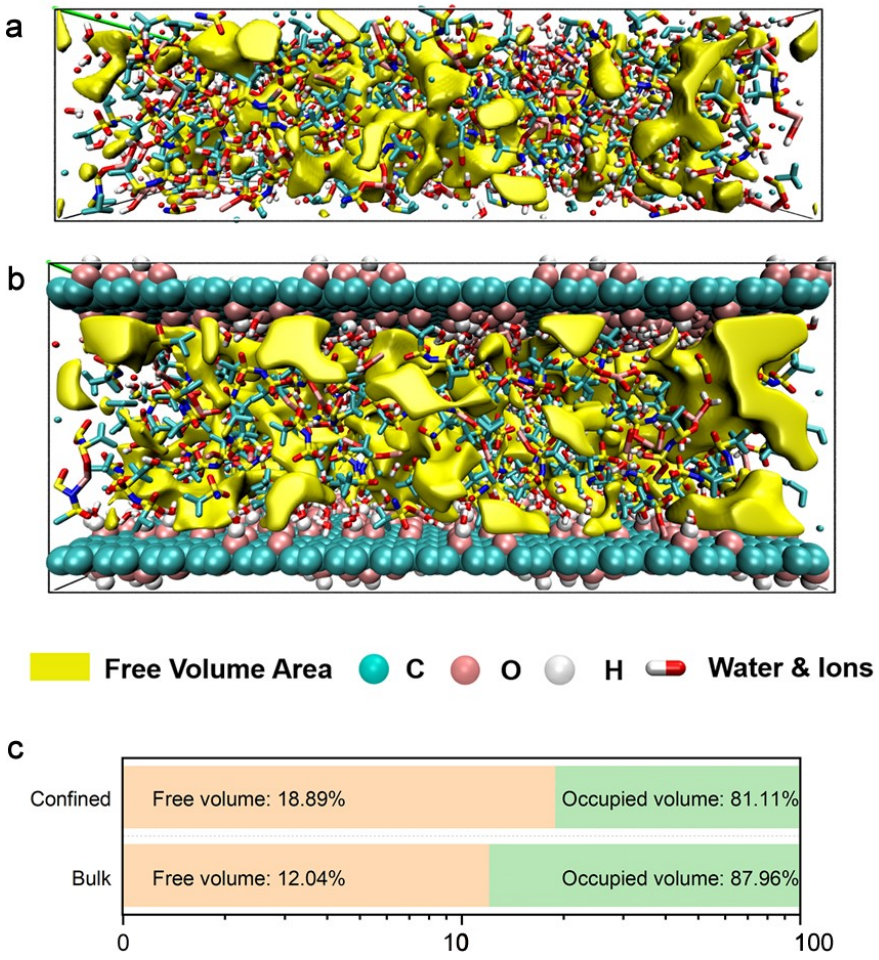

Fig. S13 The free volume simulation. (a) bulk and (b) nanoconfined model and (c) their free volume fraction comparison.

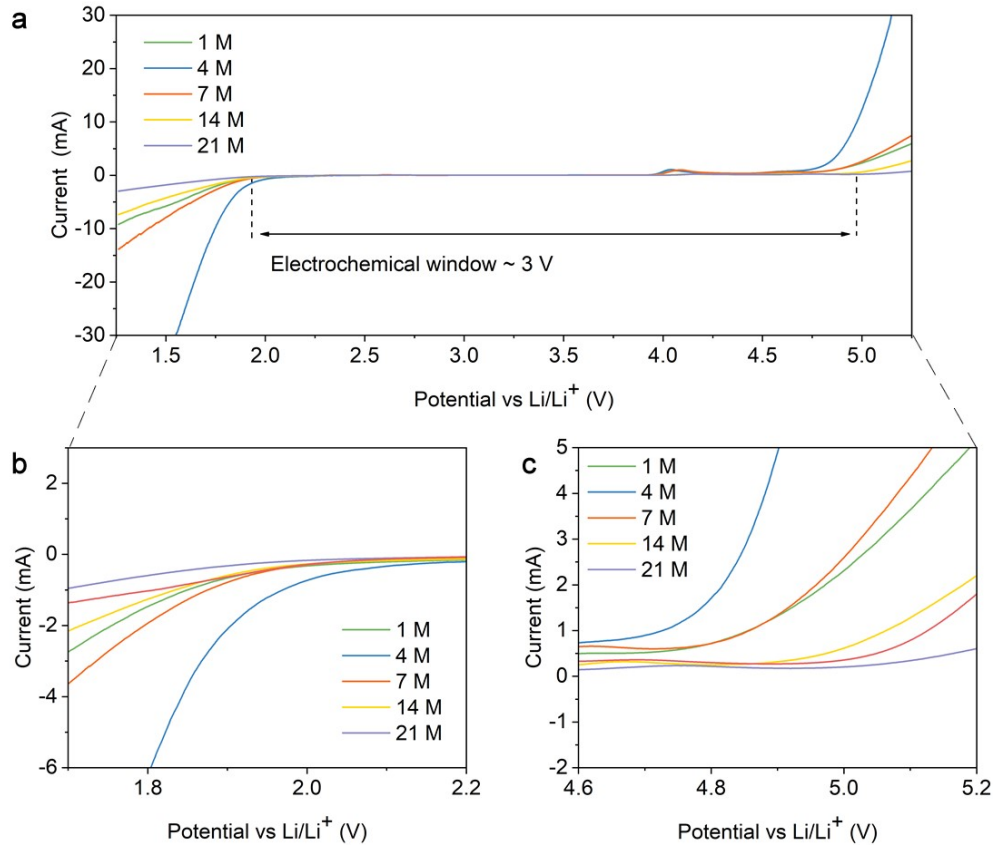

Fig. S14 The electrochemical stability window of LiTFSI bulk solution on stainless steel working electrodes where the potential has been converted to Li/Li^+ reference. (a) Overall electrochemical stability window. (b-c) Magnified view of the anodic and cathodic area.

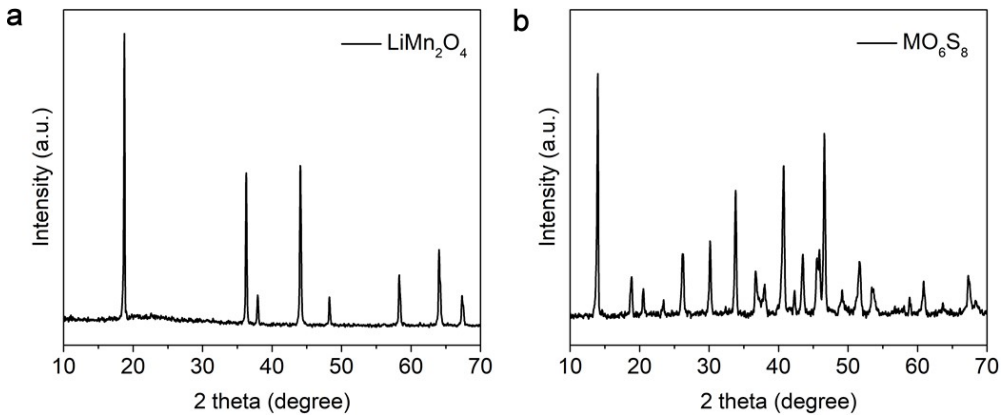

Fig. S15 XRD patterns of active materials. (a) $LiMn_2O_4$ cathode materials. (b) Mo_6S_8 anode materials.

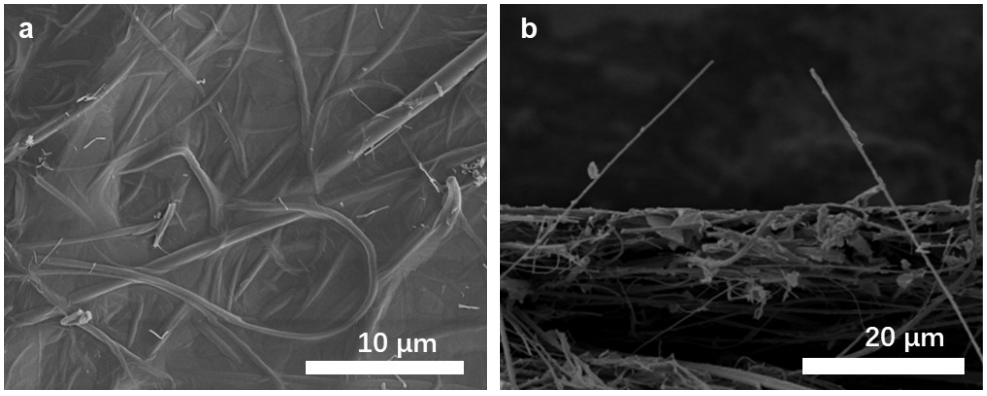

Fig. S16 SEM images of GO coated separator. (a) surface and (b) cross-section view of GO evenly coated on glass fiber.

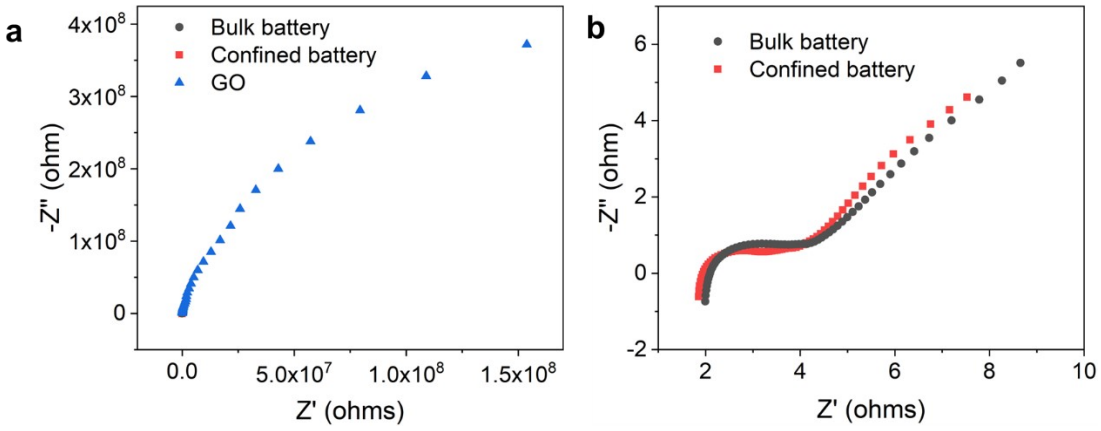

Fig. S17 The electrochemical impedance spectroscopy (EIS) test of Bulk battery, confined battery, and GO membrane.

The charge transfer resistances of GO is 10^9 higher than batteries, which could be regarded as non-conductive material in this case, and the charge transfer resistances of the confined battery (1.98 Ω) is 27% less than the bulk battery (2.7 Ω) to enable rapid charge transfer, which may suppress lithium dendrites during long-term cycling.

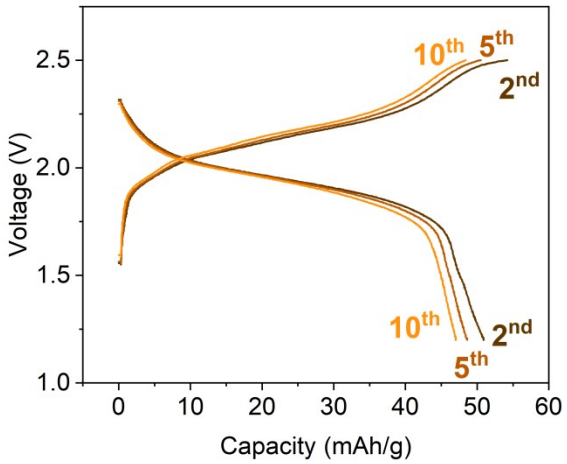

Fig. S18 The charge-discharge profiles of full aqueous lithium-ion battery based on $LiMn_2O_4$ and Mo_6S_8 at 0.5 C in GO-confined 21M LiTFSI electrolyte.

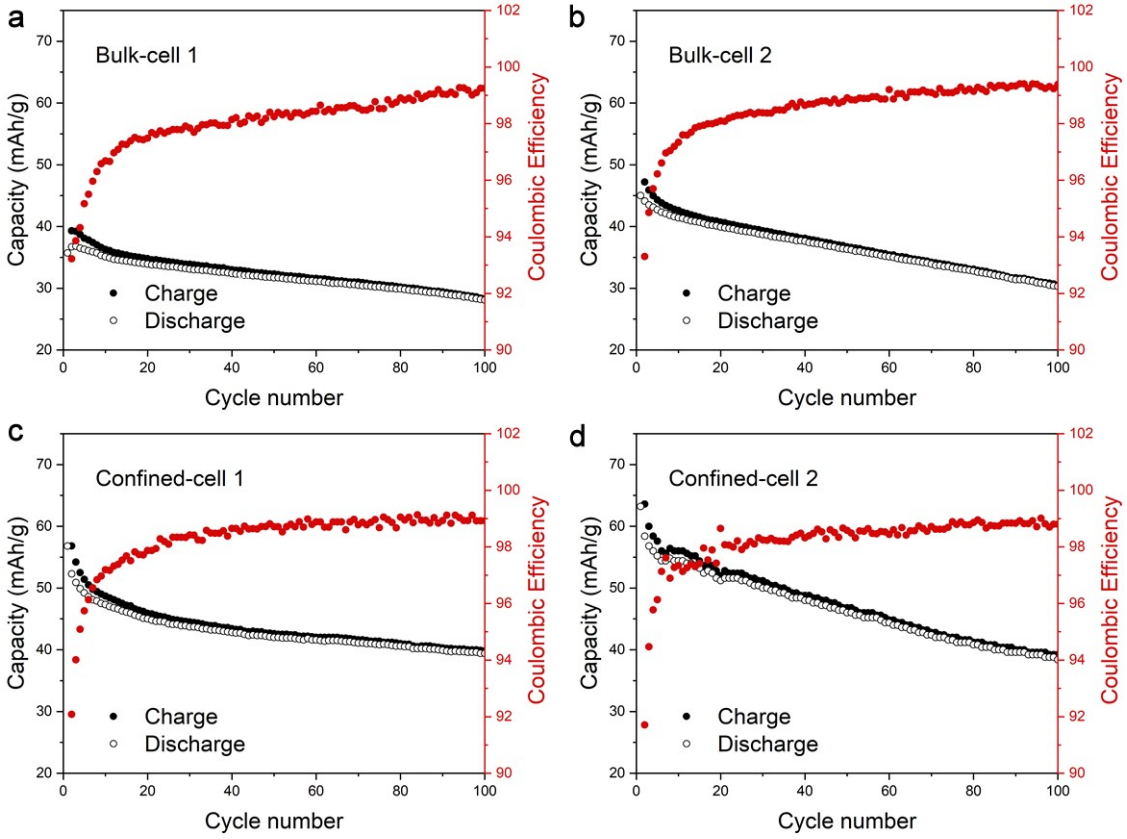

Fig. S19 The reproducibility of the (a-b) bulk and (c-d) GO-confined full aqueous lithium-ion battery at 0.5Ce in 21M LiTFSI electrolyte.

References

1 S. Xia, M. Ni, T. Zhu, Y. Zhao and N. Li, *Desalination*, 2015, **371**, 78–87.

2 M. Hu and B. Mi, *Environ. Sci. Technol.*, 2013, **47**, 3715–3723.

3 L. Suo, O. Borodin, T. Gao, M. Olguin, J. Ho, X. Fan, C. Luo, C. Wang and K. Xu, *Science*, 2015, **350**, 938–943.

4 M. Zhang, K. Guan, Y. Ji, G. Liu, W. Jin and N. Xu, *Nat. Commun.*, 2019, **10**, 1–8.

5 F. Fornasiero, H. G. Park, J. K. Holt, M. Stadermann, C. P. Grigoropoulos, A. Noy and O. Bakajin, *Proc. Natl. Acad. Sci.*, 2008, **105**, 17250–17255.

6 L. Jiang, F. Cheng, J. Chen, H. K. Liu and S. X. Dou, *Nano Energy*, 2017, **33**, 205–212.

7 R. B. Schoch, J. Han and P. Renaud, *Rev. Mod. Phys.*, 2008, **80**, 839–883.

8 K. Raidongia and J. Huang, *J. Am. Chem. Soc.*, 2012, **134**, 16528–16531.

9 C. Cheng, G. Jiang, G. P. Simon, J. Z. Liu and D. Li, *Nat. Nanotechnol.*, 2018, **13**, 1–6.

10 Z. Zhao, S. Ni, X. Su, Y. Gao and X. Sun, *ACS Sustain. Chem. Eng.*, 2019, **7**, 14874–14882.